J. Fluid Mech. (1998), *vol.* 363, *pp.* 79–96. Printed in the United Kingdom

Vortical patterns behind a tapered cylinder oscillating transversely to a uniform flow

By A. H. TECHET, F. S. HOVER, AND M. S. TRIANTAFYLLOU

Department of Ocean Engineering, Massachusetts Institute of Technology, Cambridge, MA 02139, USA

(Received 19 June 1997 and in revised form 18 December 1997)

Visualization studies of the flow behind an oscillating tapered cylinder are performed at Reynolds numbers from 400 to 1500. The cylinder has taper ratio 40:1 and is moving at constant forward speed U while being forced to oscillate harmonically in the transverse direction. It is shown that within the lock-in region and above a threshold amplitude, no cells form and, instead, a single frequency of response dominates the entire span. Within certain frequency ranges a single mode dominates in the wake, consisting of shedding along the entire span of either two vortices per cycle ('2S' mode), or four vortices per cycle ('2P' mode); but within specific parametric ranges a *hybrid mode* is observed, consisting of a '2S' pattern along the part of the span with the larger diameter and a '2P' pattern along the part of the span with the smaller diameter. A distinct vortex split connects the two patterns which are phase-locked and have the same frequency. The hybrid mode is periodic, unlike vortex dislocations, and the location of the vortex split remains stable and repeatable, within one to two diameters, depending on the amplitude and frequency of oscillation and the Reynolds number.

1. Introduction

The topology of vortical pattern formation behind oscillating uniform and tapered cylinders in a uniform stream is a subject of great theoretical and practical interest. The flow around a circular cylinder has become the canonical problem of flow around bluff bodies, presenting very rich dynamic behaviour despite its geometric simplicity. Applications are many in diverse systems involving structural and acoustic vibrations. A smoothly tapered cylinder introduces a geometry that is a perturbation from a nominally two-dimensional one, and hence constitutes an important step in assessing systematically the effects of geometric changes and, equivalently, flow shear. Despite efforts spanning several decades, there are still unmapped physical mechanisms of vortex formation even for uniform cylinders, especially for higher Reynolds numbers.

Gaster (1969, 1971) studied the flow behind a stationary tapered cylinder, noting the formation of spanwise cells within which shedding frequency is constant. Stansby (1976) has studied the flow structure behind rigid cylinders in shear flow. He noted the formation of cells of constant frequency; the length of the cells depends on the amplitude of oscillation. When the cylinder is stationary several cells form, but as the amplitude increases a dominant middle cell appears, with smaller cells forming near the ends. At sufficiently large amplitude, and within the lock-in region, a single cell dominates; the phase of vortex shedding varies continuously along the span, however.

Papangelou (1992), Piccirillo & Van Atta (1993) and Anderson & Szewczyk (1995) have studied the flow behind stationary tapered cylinders in uniform flow. Piccirillo & Van Atta (1993) noted the formation of spanwise cells of constant vortex shedding, whose non-dimensional length scales with the taper ratio but is nearly independent of the Reynolds number for $Re > 100$. A model of cell formation has been proposed by Noack, Ohle & Eckelmann (1991).

Williamson & Roshko (1988) provided a clear picture of the patterns forming behind an oscillating cylinder with uniform section, as a function of amplitude and frequency of oscillation, and for Reynolds numbers in the range 300–1000. The force phase discontinuity and hysteresis effects noted in experiments, such as for rigid oscillating cylinders by Bishop & Hassan (1964) and Feng (1968), and for vibrating cables by Brika & Laneville (1993), can be explained in terms of the transition from two vortices per cycle (the '2S' mode characterized by the formation of two single, opposite-sign vortices per cycle) to four vortices per cycle (the '2P' mode consisting of two pairs of counter-rotating vortices per cycle). Ongoren & Rockwell (1988*a*, *b*) study the wake structure and timing of shedding in an oscillating cylinder and cover in detail cases outside the synchronization regime where no single mode emerges and, instead, mode competition and switching dominate. Nakano & Rockwell (1994) show that if the imposed motion is amplitude-modulated, substantial changes can be achieved in the structure of the near and far wake, compared to the case of a purely sinusoidal motion.

Bloor (1964) studied the instability of the shear layers emanating from the cylinder, which results in the formation of secondary vortices. Similar features were noted by other authors, including, more recently, Prasad & Williamson (1997). When the primary Kármán vortices are shed parallel to the cylinder axis, the transition Reynolds number at which the secondary instability is first observed, is about 1200; under oblique shedding conditions the critical Reynolds number varies substantially.

Roshko (1954) identified the transition to irregular vortex shedding to be in the range of Reynolds numbers between 150 and 300. Recently, investigation of three-dimensional patterns in nominally two-dimensional flows has shed much light on the physical mechanisms, particularly at low Reynolds numbers. Coutanceau & Defaye (1991) have provided a detailed overview of the shedding process for stationary and moving cylinders, covering a very extensive literature. Williamson (1996*a*) reviews the cascade of phenomena appearing as Reynolds number is increased from the stable laminar range $Re < 49$, to supercritical values $Re > 10^6$. The three-dimensional transition of the wake starts at $Re \approx 190$ with the formation of modes A and B in Williamson's nomenclature; mode B dominates after $Re \approx 250$ and results in the formation of streamwise vortices with a typical distance of one diameter from each other. These rib-like structures connect and wrap around the Kármán vortices; they have been studied by Wei & Smith (1986), Bays-Muchmore & Ahmed (1993), Wu *et al.* (1994, 1996), Szepessy (1994), Towfighi & Rockwell (1994), Chyu & Rockwell (1996), and at higher Reynolds numbers by Lin, Vorobieff & Rockwell (1996), and Zhou & Antonia (1994), among others. The streamwise vortices scale with the Kármán vortices even when shear layer (Bloor) vortices are present. Triantafyllou (1992) considered theoretically the problem of three-dimensional patterns in a nominally two-dimensional wake; Karniadakis & Triantafyllou (1992) studied the same problem numerically, finding the wake inherently three-dimensional for $Re > 200$.

Vortex dislocations (also called, equally descriptively, vortex splitting), i.e. the strong localized distortions of a spanwise vortex and its connection with two or more vortices, have been studied by Gerrard (1978), Eisenlohr & Eckelmann (1989), Williamson

(1992) and Zhang *et al.* (1995). Williamson (1992) has shown that vortex dislocations account for intermittent low-frequency oscillations in the wake. Such vortex dislocations are generated between adjacent spanwise cells of different frequency and cause a momentary difference in shedding phase of the primary vortices between cells. Cells are caused, for example, by cylinder inhomogeneities and by end conditions.

The patterns behind a tapered cylinder cannot be expected to compare with those of a uniform cylinder, since its diameter varies along the length. This raises the question: what, if any, is the predominant vortical pattern behind an oscillating tapered cylinder, and how does it vary along the span. To address this question, we conducted a systematic set of visualization tests using a tapered cylinder. Above a threshold amplitude and within certain frequency ranges, a single vortical pattern was observed to emerge clearly, and there were no discernible cells of vortex formation. We attribute this difference from stationary cylinders to the effect of amplitude of vibration. This is in agreement with the findings by Stansby (1976), who, as mentioned above, noted that increased amplitude of oscillation tended to alter drastically the length of the forming cells, and to result in the formation of a dominant middle cell. Lead precipitation and DPIV methods illuminated some new features in the wake of the 40:1 tapered cylinder. A *hybrid mode* was observed throughout the Reynolds number range considered, i.e. between 400 and 1500, based on an average diameter of the cylinder, $\overline{d} = 2.4$ cm. This phenomenon constitutes a new mechanism peculiar to oscillating tapered cylinders in uniform flow, and by extension possibly to uniform cylinders in shear flow.

2. Experimental methods

Visualization experiments were performed at the MIT Testing Tank Facility. A tapered test section was towed at steady forward speed while oscillating in the transverse direction, and the vortical patterns were recorded. First, an electrolytic precipitation method provided insight into the qualitative behaviour of the wake as function of the amplitude and frequency of oscillation. Then, digital particle image velocimetry (DPIV) provided quantitative data of the instantaneous velocity field and its associated vorticity along a plane of interrogation.

2.1. *Flow-visualization set-up*

The flow-visualization experiments were conducted in a glass tank with dimensions 2.4 m $\times$ 0.75 m $\times$ 0.75 m. A motor-driven carriage moves along the top of the tank at constant speed, up to 20 cm s^{-1}, driven by an AC motor. An oscillating mechanism is mounted on top of the carriage, forced by a DC motor, which imposes forced harmonic oscillation with amplitudes up to 7.62 cm. The scotch-yoke four-bar linkage mechanism is detailed in Gopalkrishnan *et al.* (1994). The frequency of oscillation can be varied continuously from 0 to 0.7 Hz by adjusting the power supplied to the motor. The layout of the apparatus is shown in figure 1.

The tapered cylinder was a wooden spar coated in a layer of lightweight fibreglass cloth. Epoxy was applied twice to increase the stiffness and avoid swelling due to water absorption. The cylinder dimensions are $d_{max} = 3.2$ cm, $d_{min} = 1.55$ cm, the average diameter, $\overline{d}$, is 2.4 cm, and the overall length of taper, l, is 66 cm. The taper ratio is defined by

$$\tau = \left| \frac{l}{d_{max} - d_{min}} \right|. \tag{2.1}$$

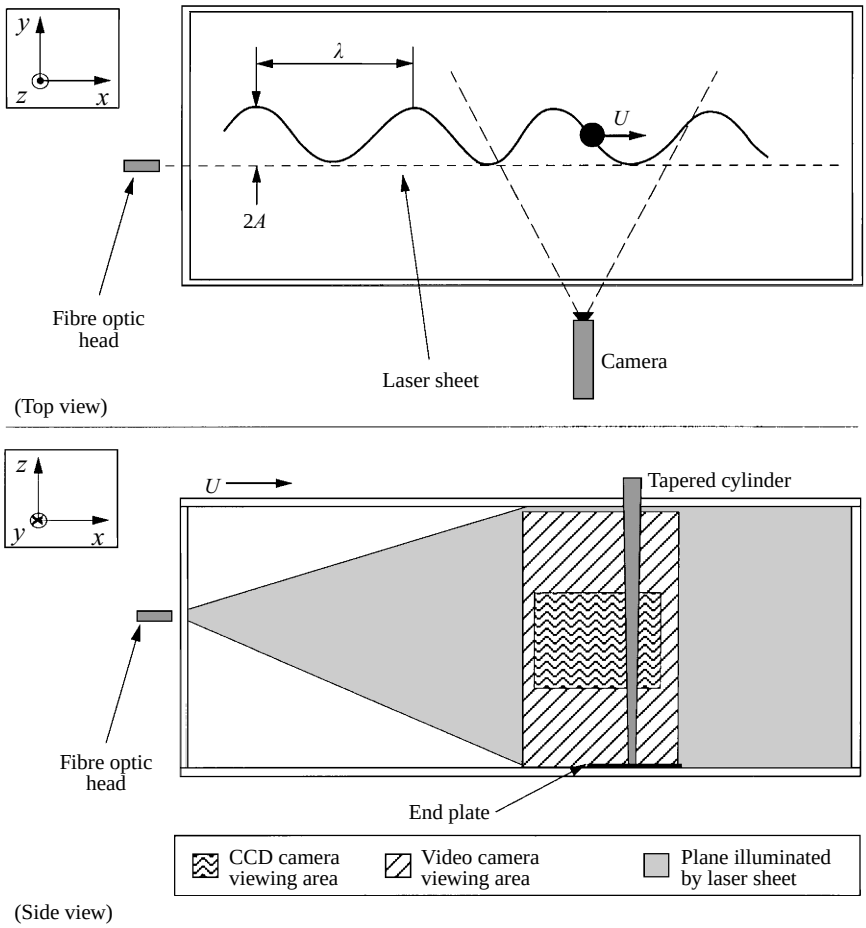

FIGURE 1. Experimental set-up: top and side views

Using this equation, the taper ratio is equal to 40:1. The cylinder reaches very close to the bottom of the tank, 72 cm deep, but the taper only extends from the bottom up to 66 cm. The cylinder was not fitted with end plates in order to facilitate visualization; the gap between the lower end of the cylinder and the bottom was less than 0.5 cm, which was found to reduce end effects to within two diameters from the lower end, in agreement with the findings by Slaouti & Gerrard (1981).

Both visualization methods employ a high-resolution black-and-white CCD video camera, Texas Instruments MULTICAM MC1134P, which recorded the flow with a maximum pixel resolution of 1134×480 pixels at a standard frame rate of 30 Hz. Dual field exposure rendered full vertical resolution with no interlace. The video from the CCD camera is stored real-time directly to a Sony CRVdisc video-disc recorder (LVR-5000A). The video frames are digitized at 8 bits/pixel by an EPIX 4MEG video board in a 486 PC. In the lead precipitation method, a standard video camera is also employed to observe the shedding patterns along the entire length of the cylinder.

A mechanical shutter was used in the DPIV experiments to reduce the exposure time of the images, thus changing the effective framing rate of the camera from 30 Hz to 15 Hz. This triggering allows the images to be grouped into pairs separated by

1.5 ms. A General Pixels Timing box synchronized to the video signal controls the laser shutter.

The seed particles in both methods are illuminated by light from a 6 W continuous beam Argon-Ion laser. The light from the laser passes through the mechanical shutter and into a fibre optic cable which extends to the experimental area. At the far end of the cable the head of the fibre optic cable spreads the laser beam into a sheet in order to illuminate an entire two-dimensional plane in the flow field. For the visualizations of the vertical planes, the laser sheet is positioned at the point of maximum oscillation and captured by the camera through the side window of the tank. For the horizontal slices, the laser sheet is placed at the location along the span which is of interest and the camera records the image through a window in the bottom of the tank.

2.2. *Lead precipitation*

Lead precipitation is used to obtain a qualitative understanding of the shedding patterns in the cylinder wake, and is a variation of the electrolytic precipitation method outlined in a paper by Honji, Taneda & Tatsuno (1980). Their method involved the coating of a test section with a tin solder, whereas our method employs a thin lead foil strip that is introduced along the stagnation line of the cylinder. This lead precipitation method is similar to that outlined in Anderson & Szewczyk (1995).

Lead precipitation is achieved by placing a strip of thin lead foil tape along the stagnation line of the cylinder and connecting it to one pole of a DC power supply. The other pole may be connected to a conducting plate, or as in the present experiments, to a section of copper tubing which serves as the cathode. This copper tubing is placed sufficiently downstream and to the side of the cylinder, such that it does not affect the vortex formation process and does not obstruct the area of flow being observed.

When a voltage differential is applied across the two poles, a cloud of lead particles precipitates into the flow. The foil tape can be moulded into any shape, thus allowing it to be smoothed into the leading edge of the cylinder and providing a non-intrusive method of flow visualization. The particles are emitted from the leading edge directly into the boundary layer of the cylinder. This makes the lead precipitation method very useful for observing the separation of the shear layer. The lead precipitate is illuminated by the 6 W Argon-Ion laser, operating at less than half power, which was found to be adequate for these experiments. In order for the lead precipitation to be successful, an additive, such as salt, is introduced to enhance the water's conductivity. Here Morton's 99.5% pure salt pellets, similar to those use in water treatment processes, were added; however simple table salt was found to produce the same results.

The images recorded by the second, standard video camera were used to record the different spanwise shedding patterns and also to determine the point at which dislocations occurred. The resolution of the second camera was occasionally not sufficient to capture certain details. The images obtained from the CCD camera yielded the needed detail, but only captured a portion of the spanwise the shedding between $z/\overline{d} = 9.75$ and 14.75. The total height of the images obtained with the CCD camera is five average diameters.

2.3. *DPIV method*

Quantitative velocity field measuring experiments were conducted using particle image velocimetry (Adrian 1991) as implemented digitally by Willert & Gharib (1991). A plane is illuminated using a laser beam fanned to form a plane sheet; and the fluid is

seeded with neutrally buoyant fluorescent particles (diameter $\approx$ 40 to 70 μm) which reflect wavelengths in the range of 560–580 nm. Willert & Gharib (1994) found that 10 to 20 particles per interrogation window were sufficient to ensure good correlations. Camera positioning must ensure that the particle images are approximately 2–3 pixels in size, since the algorithm cannot resolve sub-pixel images. Image data from two successive video frames are collected and stored digitally in levels of greyscale. In each of the frames we examine small interrogation windows at the same spatial position and the data are used to calculate the cross-correlation function which provides a measure of goodness of match between images. A strong narrow peak in the correlation function provides the average displacement of the sampled group of particles. The effect of the DPIV windowing process is that of a spatial low-pass filter. Using the analysis in Willert & Gharib (1991), we observe a 40% attenuation of features on the order of 64 pixels when a 32 $\times$ 32 window is used in the processing. The attenuation is limited to less than 10% for features nearing 160 pixels in size. Similarly, for a 16 $\times$ 16 processing window, features on the order of 32 pixels are attenuated by approximately 35%, and a 10% attenuation is realized for features near 75 pixels in size. We estimate a mean relative RMS error of 5–6% for particle displacements in the range of 0–9 pixels; absolute errors ranged from 0.01 pixels to 0.15 pixels. Increased seeding densities beyond 20 particles per 32 $\times$ 32 window show no significant improvement in uncertainty. A typical relative RMS error for moderate pixel excursions (greater than 1 pixel) is of the order of 5%. In terms of velocity this results in typical absolute error of 0.2 cm s^{-1} for a time step of 20 ms, resulting in a relative velocity error of 7.5%.

3. Results and discussion

The form of the patterns behind a uniform cylinder, forced to oscillate harmonically transversely to an oncoming stream, has been mapped by Williamson & Roshko (1988). The patterns have been found to vary significantly as function of the amplitude and frequency. For a given experiment, the patterns are expected to persist along the entire span when proper care is taken to avoid end effects, for example with the use of sufficiently sized and properly shaped end plates. Inhomogeneities along the span and end effects cause vortex dislocation and oblique shedding phenomena (Williamson 1996*b*).

Since the diameter varies along the length, the patterns in the wake of an oscillating tapered cylinder cannot be expected to compare with those of a uniform cylinder. For a given amplitude and oscillation frequency, the smaller diameter end of the cylinder will map into one regime whereas the larger diameter end will map into another, different, shedding regime in the A/d vs. λ/d plane, where $\lambda = U/f$. To discern what is the predominant vortical pattern behind an oscillating tapered cylinder, and how it varies along the span, we conducted a systematic set of visualization tests using the tapered cylinder.

For certain values of the amplitude of vibration, A/d, and the reduced frequency, $f^* = fd/U$, we observed a *hybrid mode* forming, consisting of, using the nomenclature of Williamson & Roshko (1988): a '2S' mode, i.e. two vortices per cycle, along the part of the cylinder span with the larger diameter; and a '2P' mode, i.e. four vortices per cycle, for the rest of the span which had smaller diameter. A distinct vortex split connected the two patterns, which had the same frequency and were phase-locked. The hybrid mode was observed throughout the Reynolds number range considered, i.e. between 400 and 1500, based on an average diameter of the cylinder, $\overline{d} = 2.4$ cm.

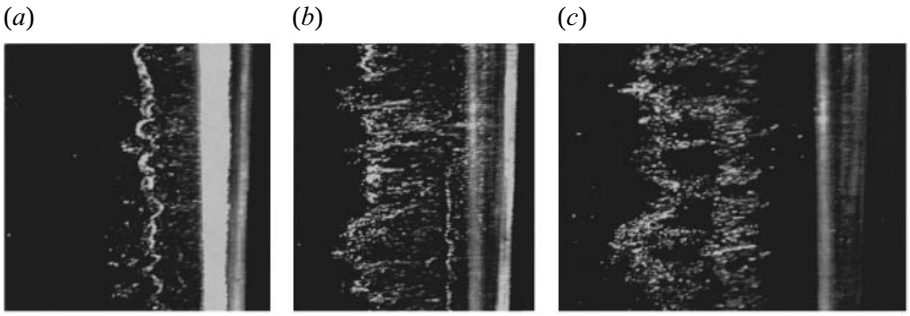

FIGURE 2. Evolution of the '2P' shedding pattern for the 40:1 tapered oscillating cylinder. $R_{\overline{d}} = 1500$, $A/\overline{d} = 0.25$, $f^* = 0.162$: (*b*) is taken 0.27 s after (*a*), and (*c*) 0.5 s later.

Spanwise and transverse visualizations, using lead precipitation and DPIV methods, illuminated the principle features in the wake of the 40 : 1 tapered cylinder.

3.1. *Spanwise visualization*

We present results here for cases demonstrating a single dominant pattern along the entire span, as well as cases showing a clear hybrid mode exhibiting pattern transition between the '2S' and '2P' mode at a location along the span of the cylinder.

A vertical plane is visualized, which is parallel to the centreline of the cylinder (z-axis) and contains the direction of the oncoming flow (x-axis), located at a distance from the average position of the cylinder (along the y-axis) equal to the maximum excursion of the edge of the average section of the cylinder. Results from both the CCD and the VHS camera are shown. Although the lead precipitation images taken using the VHS camera are less clear in detail, they are quite insightful because they show the entire span of the cylinder. Tests shown here are for two different values of the Reynolds number, $R_{\overline{d}} = 400$ and 1500; three values of amplitude to average diameter ratio, $A/\overline{d} = 0.25$, 0.5, and 1.0; and three values of the reduced frequency, $f^* = 0.162$, 0.18, and 0.198.

In figures 2–5, the tapered cylinder is moving at constant speed from left to right; the images are captured with the CCD camera. The section of cylinder span shown is about five diameters in length, stretching between $z = 9.75\ \overline{d}$ and $z = 14.75\ \overline{d}$.

Figure 2 provides three successive snapshots of the formation of a '2P' structure for higher Reynolds number, $R_{\overline{d}} = 1500$. This same pattern was observed for lower Reynolds number cases, $R_{\overline{d}} = 400$ to $R_{\overline{d}} = 1500$, as well. In this figure the amplitude to diameter ratio is $A/\overline{d} = 0.25$ and the reduced frequency $f^* = 0.162$. The first figure (*a*) shows the first spanwise vortex being formed as the cylinder has gone through its position of maximum amplitude. Local fluctuations caused by the growth of streamwise vortices at the edge of the vortical structure, are apparent. Figure 2 (*b*), 0.27 s (8 frames) later, shows the same vortex completely formed and located at a new position downstream, while it reveals the emergence of the second spanwise vortical structure, which appears as a thin bright line between the previous vortex and the cylinder. At the next time step shown in figure 2 (*c*), 0.5 s later, the second vortex has also fully formed. Streamwise vortical structures, spaced about one cylinder diameter apart, take shape connecting and wrapping around the two counter-rotating vortices; these cause the helical contortions in the first vortex to grow.

The influence of the streamwise vortices is also evident in the three cases shown in figure 3. Several smaller vortices connect in the streamwise direction and wrap

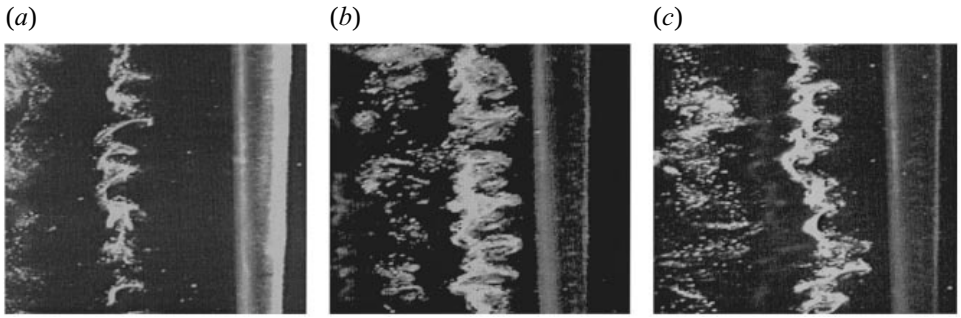

FIGURE 3. Streamwise vortices are seen for the 40:1 tapered oscillating cylinder in '2P' mode at $R_{\bar{d}} = 400$. (a) $A/\bar{d} = 0.5$, $f^* = 0.198$; (b) $A/\bar{d} = 1.0$, $f^* = 0.162$; and (c) $A/\bar{d} = 1.0$, $f^* = 0.18$.

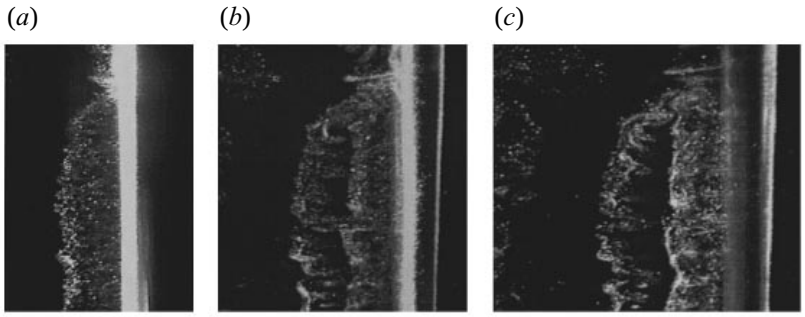

FIGURE 4. Hybrid mode shown at the spanwise location of pattern transition from '2S' to '2P' pattern: three successive snapshots for $R_{\bar{d}} = 400$, $A/\bar{d} = 0.5$, $f^* = 0.198$.

around the two main vortices, contorting their shape to appear almost helical. In each case the cylinder has just passed from the position of maximum displacement and is moving towards the centreplane. Shedding is dominated by the '2P' pattern in all cases for $R_{\bar{d}} = 400$. Figure 3 (*a*) is obtained for $A/\bar{d} = 0.5$ and reduced frequency $f^* = 0.2$; figure 3 (*b*) for $A/\bar{d} = 1.0$ and reduced frequency $f^* = 0.162$ and figure 3 (*c*) for $A/\bar{d} = 1.0$ and reduced frequency $f^* = 0.18$. In figures (*b*) and (*c*), adjacent streamwise vortices, which are counter-rotating, have the appearance of 'mushroom' structures superposed on the main vortex line to the right. Also in figures (*a–c*), as the pair of spanwise counter-rotating vortices convects laterally away from the centreline of oscillation, the first vortex has convected further out of the visualization plane, in the direction away from the average position of the cylinder, and is less clearly visible.

Figure 4 depicts three successive snapshots from a case exhibiting hybrid mode formation. The field of view contains the transition between the '2S' pattern (upper end, larger diameter) to the '2P' pattern (lower end, smaller diameter). Figure 4 (*a*) shows the appearance of a first vortex, although there is a marked phase difference in the vortex formation at a point close to the top. The phase difference is caused by the upstream influence (memory effects) of previously shed vorticity, which has different structure at the upper and lower cylinder ends. Figure 4 (*b*) shows that a second vortex has appeared, which, however, extends only to the point where the phase difference was observed in (*a*). Further up, the second vortex acquires a three-dimensional shape, outside the plane of view and towards the centreline, connecting to a vortex which

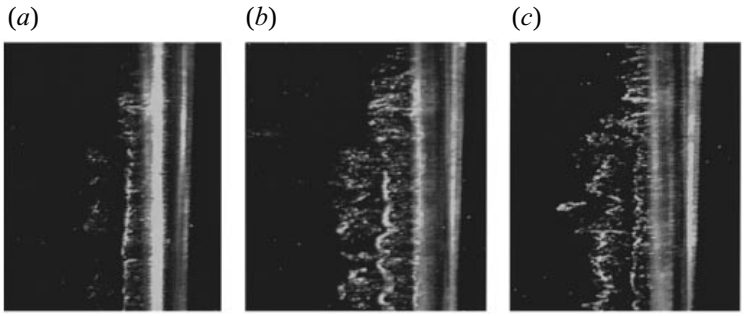

FIGURE 5. Hybrid mode shown at the spanwise location of pattern transition from '2S' to '2P' pattern: three successive snapshots for $R_{\bar{d}} = 1500$, $A/\bar{d} = 0.5$, $f^* = 0.18$.

has the same sign but lies at the opposite lateral edge of the wake. Figure 4(*c*) shows the subsequent evolution of the vortical structure, as well as the streamwise vortices which grow from (*a*) to (*c*). The Reynolds number is $R_{\bar{d}} = 400$, the amplitude to diameter ratio $A/\bar{d} = 0.5$, and the reduced frequency $f^* = 0.198$. A similar vortical structure, formed one period earlier, can be faintly seen at the left edge of figure 4(*c*); the process is repeatable from cycle to cycle.

Figure 5 depicts the portion of a hybrid mode around the spanwise location of pattern transition, for higher Reynolds number, $R_{\bar{d}} = 1500$, amplitude to diameter ratio $A/\bar{d} = 0.5$, and reduced frequency, $f^* = 0.18$. The pattern transition is found here at a slightly lower point along the span than in figure 4; also, due to the difference in the reduced frequency, the sequence in the formation of the two vortices is slightly different: in (*a*) the first vortex is faintly seen, while the second vortex is clearly seen. Figures 5(*b*) and 5(*c*) are very similar in their qualitative features to the previous figure, despite the difference in Reynolds number. More intense fluctuations in the flow are noted, however.

Next, in figures 6–8 we show images captured using the VHS camera. The entire span of the cylinder can be seen in these images.

Figure 6 shows lead precipitation images, demonstrating the formation of hybrid modes for $A/\bar{d} = 0.25$, two Reynolds numbers $R_{\bar{d}} = 400$ and 1500, and three values of the reduced frequency, $f^* = 0.162$, 0.18 and 0.198. The vortical structure clearly consists of '2S' and '2P' patterns joined through vortex splitting. Previously shed vortices have increasingly more three-dimensional structure and appear less clear; however they retain their original structure. For both values of Reynolds number the location of pattern transition moves towards the lower end as the reduced frequency decreases from a value of 0.162 to a value of 0.198. For Reynolds number 400, for $f^* = 0.162$ the split occurs at $z/\bar{d} = 21.0$, where z is measured from the lower end, for $f^* = 0.18$ at $z/\bar{d} = 20.1$, and for $f^* = 0.198$ at $z/\bar{d} = 17.3$. For Reynolds number 1500, for $f^* = 0.162$ the split occurs at $z/\bar{d} = 19.8$, for $f^* = 0.18$ at $z/\bar{d} = 16.2$, and for $f^* = 0.198$ at $z/\bar{d} = 15.3$. The heights of the splits were resolved within (plus or minus) one average diameter.

Figure 7 shows lead precipitation images, again demonstrating the formation of hybrid modes, for $A/\bar{d} = 0.5$, two Reynolds numbers $R_{\bar{d}} = 400$ and 1500, and three values of the reduced frequency, $f^* = 0.162$, 0.18 and 0.198. Results are qualitatively similar to the previous cases, shown in figure 6, which depicted hybrid modes for a lower amplitude; however, the location of transition shifts to lower spanwise locations, as expected from quasi-two-dimensional considerations of the effect of

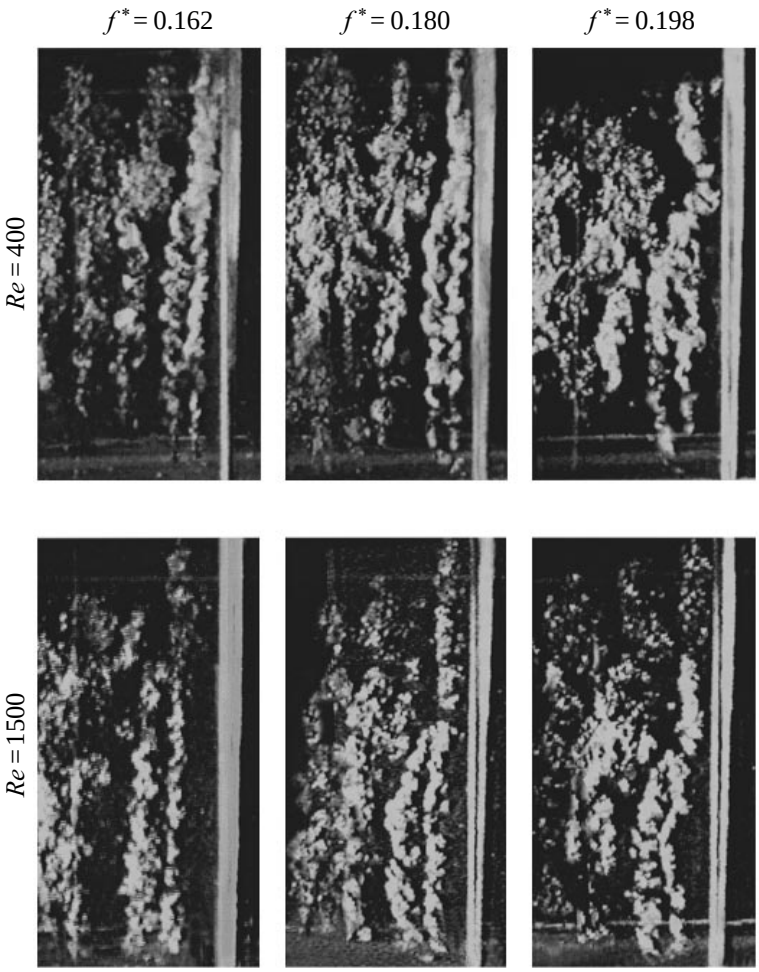

FIGURE 6. Lead precipitation visualization showing the entire cylinder span for $A/\overline{d} = 0.25$.

amplitude using the results of Williamson & Roshko (1988) for uniform cylinders. Also, the Reynolds number appears to have an effect on the spanwise location of the pattern transition. Again, for both values of Reynolds number the location of pattern transition moves towards the lower end as the reduced frequency decreases from a value of 0.162 to a value of 0.198. For Reynolds number 400, for $f^* = 0.162$ the split occurs at $z/\overline{d} = 23.2$, where z is measured from the lower end, for $f^* = 0.18$ at $z/\overline{d} = 20.7$, and for $f^* = 0.198$ at $z/\overline{d} = 17.0$. For Reynolds number 1500, for $f^* = 0.162$ the split occurs at $z/\overline{d} = 21.2$, for $f^* = 0.18$ at $z/\overline{d} = 15.1$, and for $f^* = 0.198$ at $z/\overline{d} = 9.0$.

Figure 8 shows lead precipitation images for $A/\overline{d} = 1.0$, two Reynolds numbers $R_{\overline{d}} = 400$ and 1500, and three values of the reduced frequency, $f^* = 0.162$, 0.18 and 0.198. Streamwise vortices are ubiquitous as before; the vortical structure, however, is definitely of a single mode, '2P', for all parametric values.

In figure 9 we present a comparison between the mode transition results of the tapered cylinder, obtained from figures 6–8 herein, and the uniform-cylinder results of Williamson & Roshko (1988), as function of the amplitude to diameter ratio A/d

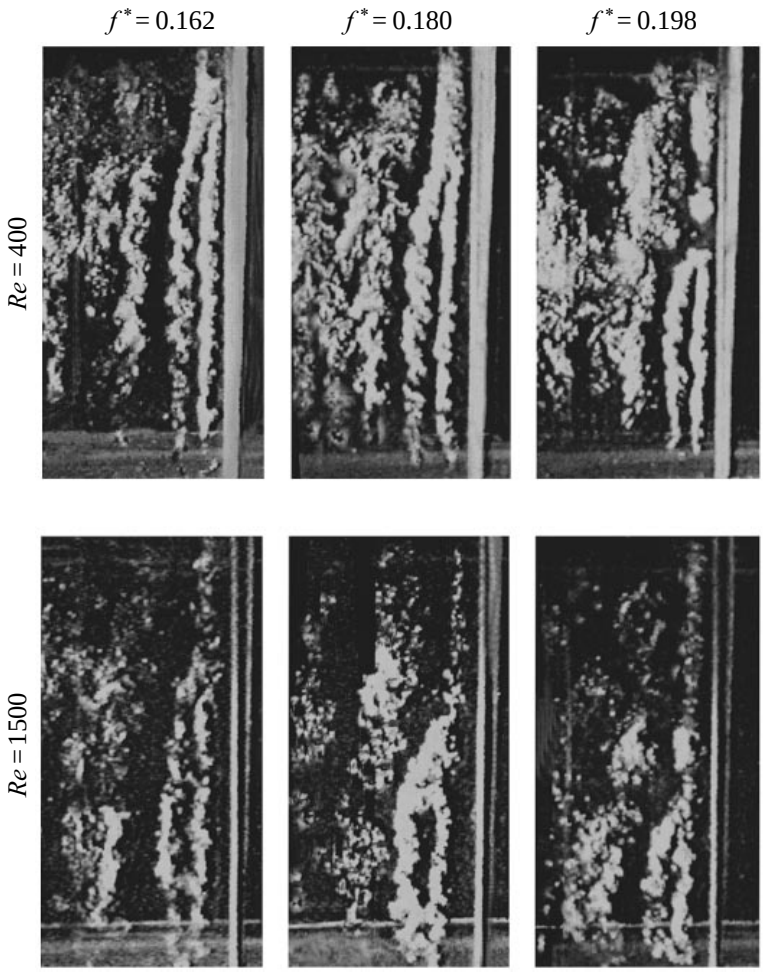

FIGURE 7. Lead precipitation visualization showing the entire cylinder span for $A/\overline{d} = 0.5$.

and reduced velocity V_r. Dashed lines mark the transitions between modes obtained by Williamson & Roshko. We provide the combinations of A/d and $V_r = U/(fd)$ corresponding to the ends of the tested cylinders for each experiment, where the actual diameter d is used, and we mark the type of vortex pattern observed: the smaller diameter end is marked by the 'o' symbol, and the larger diameter end by the '$*$' symbol. For the cases where a hybrid mode is observed, we mark the corresponding location of the vortex split, based on the local diameter. Because the split can be identified within one diameter (plus or minus) and there is Reynolds number dependence, we provide a shaded patch rather than a discrete line. As seen, there is reasonable agreement between the data obtained for the linearly tapered cylinders herein, and the uniform-cylinder data of Williamson & Roshko.

3.2. *Visualization at planes perpendicular to the cylinder axis*

Visualization across planes perpendicular to the cylinder axis, i.e. (x, y)-planes, are recorded to compare with the patterns observed behind uniform cylinders. The lead precipitation method and DPIV were employed for this purpose. In the cases using lead precipitation, the tank was also seeded with fluorescent particles used in DPIV,

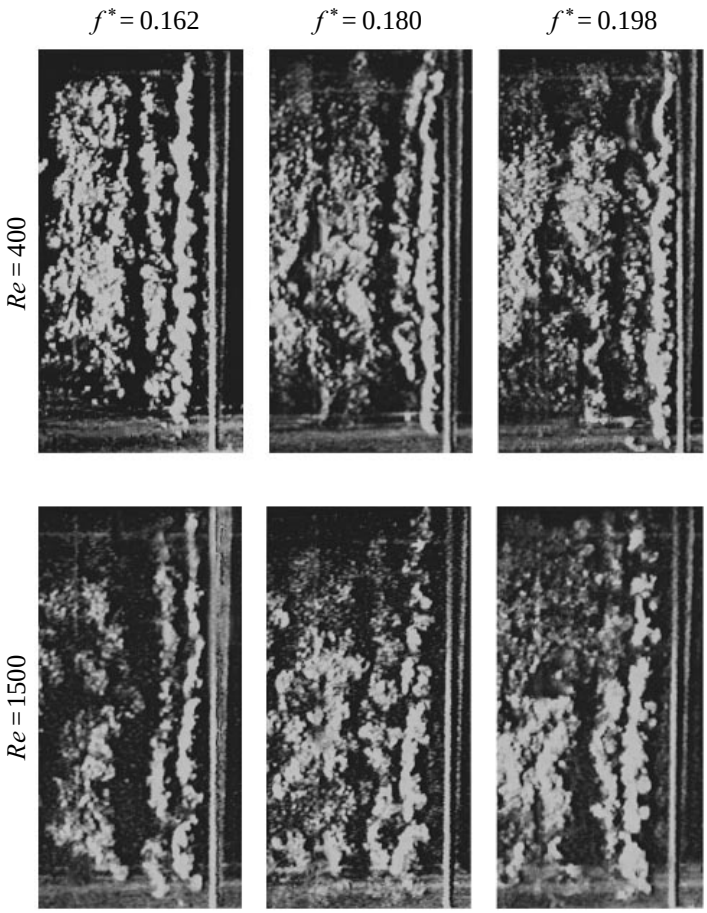

FIGURE 8. Lead precipitation visualization showing the entire cylinder span for $A/\overline{d} = 1.0$.

which enhanced the visualization process and allowed several of the cases to be processed using the DPIV algorithm. Using the vertical images (x, z-plane) as a reference, perpendicular (x, y-plane) slices were taken above and below the transition in shedding mode. Both Reynolds numbers 400 and 1500 showed distinct '2S' and '2P' patterns, above and below the transition, respectively. An additional set of experiments, at the intermediate Reynolds number 800 was also investigated for comparison.

At the two lower Reynolds numbers, 400 and 800, the formation and evolution of the two patterns was clear. For $R_{\overline{d}} = 1500$ the presence of shear layer vortices was noted, making visualization less clear; yet the two different patterns can still be established unambiguously.

Figure 10 provides two snapshots of the formation of a '2P' mode for $R_{\overline{d}} = 1,500$, $A/\overline{d} = 0.5$, $f^* = 0.18$ showing shear layer vortices forming on the layers emanating from the cylinder. In figure 10 (a) the slice is at $z/\overline{d} = 6.5$, well below the pattern transition region. The image is taken when the cylinder has fully traversed through its maximum oscillation and shed a pair of counter–rotating vortices. Figure 10 (b) is at $z/\overline{d} = 10.4$, still below the pattern transition, and taken when the cylinder has passed through the minimum oscillation and shed a pair of counter-rotating vortices at the opposite wake side to that shown in (a).

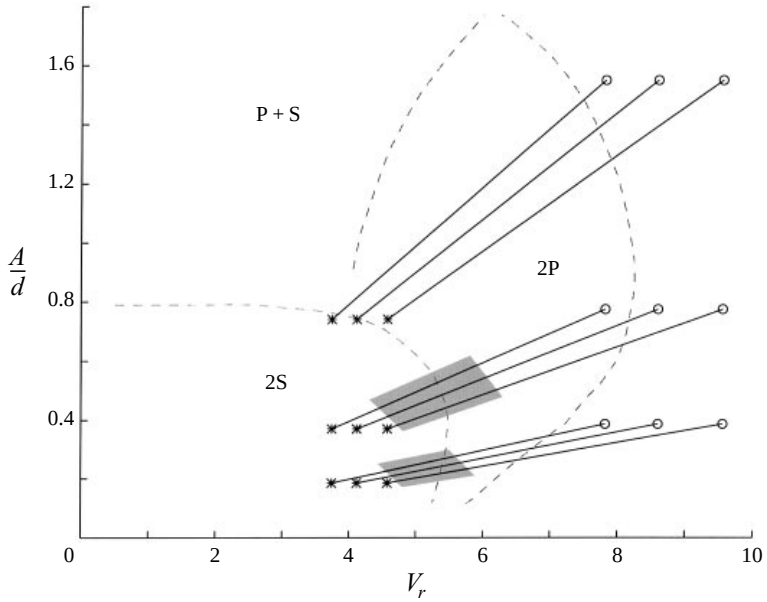

FIGURE 9. Range of reduced velocity versus amplitude to diameter ratio for the 40 : 1 tapered cylinder experiments: ∗ indicates the larger end of the cylinder and ∘ the smaller end. The shaded region represents the area of the switch in shedding mode for both Reynolds number cases: 400 and 1500. Dashed lines mark the mode transitions obtained by Williamson & Roshko.

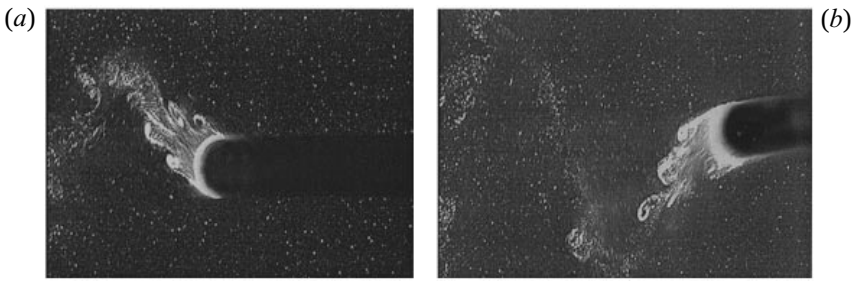

FIGURE 10. Shear layer vortices forming at $R_{\bar{d}} = 1500$, associated with a '2P' pattern. (*a*) $z/d = 6.5$, (*b*) $z/d = 10.4$.

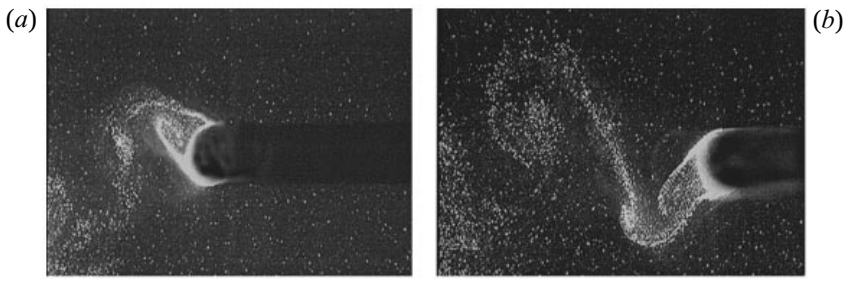

FIGURE 11. '2P' shedding mode at $R_{\bar{d}} = 400$. Image (*a*) shows the formation of a vortex pair in a '2P' pattern. Image (*b*) is taken at a later time, showing a streamwise vortex in the field of view, which connects two clockwise rotating vortices.

Figure 11 shows the formation of '2P' mode at $R_{\overline{d}} = 400$, $A/\overline{d} = 0.5$, and $f^* = 0.18$. Figure 11 (*a*) shows the beginning of shedding a pair of primary vortices at the upper edge of the wake: the first vortex is rotating counter-clockwise and the second vortex, closest to the cylinder, is rotating clockwise. The cylinder has just passed through its maximum oscillation. Figure 11 (*b*) shows a later time step for the same parametric values, as a pair of vortices is almost completely shed at the lower edge of the wake. The cylinder is travelling from the point of minimum excursion towards the centreline of oscillation. Here, coincidentally, a streamwise vortex has been captured as a bright line connecting two clockwise rotating vortices (the second and third vortices, counting as one moves downstream from the cylinder). The streamwise vortex is clearly visible when the video recording is played back; in still photographs the depiction of the primary vortical patterns is less clear (for example, the third vortex is almost indistinguishable).

Next we provide DPIV images obtained at planes transverse to the cylinder axis. They depict modes dominated by a single pattern as well as hybrid modes.

Figure 12 shows (*a*) the velocity and (*b*) the vorticity fields, obtained through DPIV and corresponding to $R_{\overline{d}} = 1500$, $A/\overline{d} = 0.5$, and $f^* = 0.18$. A '2P' pattern is clearly seen in the vorticity map (*b*). The red colour represents positive vorticity, counter-clockwise rotation of the fluid; and the blue spots show negative vorticity, clockwise rotation of the flow. The laser sheet was placed below the pattern transition region at a height: $z/\overline{d} = 6.7$. Here the cylinder has passed through its minimum oscillation and is moving up towards the centreline.

Figure 13 shows plane cuts of the velocity and vorticity fields for slices depicting a hybrid mode. Two horizontal slices have been processed, one obtained at $z/\overline{d} = 22.9$ (figures *a*, *b*), and the other at $z/\overline{d} = 7.9$ (figures *c*, *d*). The parameters are: Reynolds number 1500, $A/\overline{d} = 0.5$, and $f^* = 0.198$. The vorticity field shown in figure 13 (*b*) shows that the upper portion of the cylinder in this case is shedding a '2S' pattern, whereas the lower slice (figure 13 *d*) shows a '2P' pattern; both figures are consistent with the lead precipitation results.

Figure 14 shows velocity and vorticity plots depicting a hybrid mode for different conditions than shown in figure 13: $R_{\overline{d}} = 1500$, $A/\overline{d} = 0.5$, and $f^* = 0.18$. The two slices are located at different heights: $z/\overline{d} = 18.7$ (figure 14 *a*, *b*) and $z/\overline{d} = 6.7$ (figure 14 *c*, *d*). Again, as in the previous figure, the upper slice depicts a '2S' pattern and the lower slice shows a '2P' pattern of shedding.

We used the velocity and vorticity plots to obtain estimates of the circulation of the vortices. This is done by integrating the vorticity inside a circular area whose centre is chosen to be within the core of the vortex, while its radius is incrementally increased until the circulation value levels off within a pre-set tolerance. Circulation in the '2S' mode (figure 14 *b*) for the clockwise vortex with its core located at $x/d = 2.8$ is $\Gamma_s = -22.13$ cm^2 s^{-1}. For the '2P' mode (figure 14 *d*), for the clockwise vortex with its core at $x/d = 2$ we find $\Gamma_{p1} = -6.3$ cm^2 s^{-1}, and for the clockwise vortex with its core at $x/d = 4$ we find $\Gamma_{p2} = -18.56$ cm^2 s^{-1}; hence the sum circulation for the two clockwise vortices in the '2P' pattern is $\Gamma_p = -25.89$ cm^2 s^{-1}. In accordance with the lead precipitation results, the two clockwise vortices from the '2P' mode considered above connect to the single clockwise vortex from the '2S' vortex at the location of the vortex split. Given the distance between the two slices and the uncertainty in evaluating the circulation, the calculation supports the suggested topology of the vortical structure.

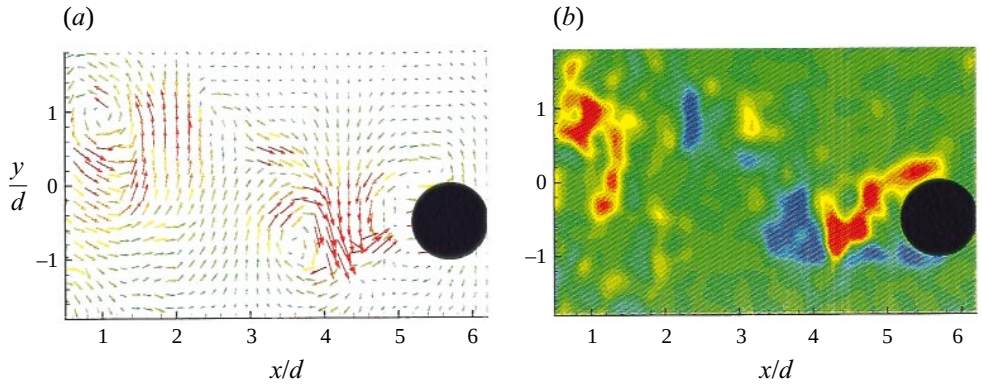

FIGURE 12. (*a*) Velocity and (*b*) vorticity plots showing a '2P' pattern for $R_{\overline{d}} = 1500$, $A/\overline{d} = 0.5$, and $f^* = 0.18$. The horizontal slice is imaged at $z/\overline{d} = 6.7$.

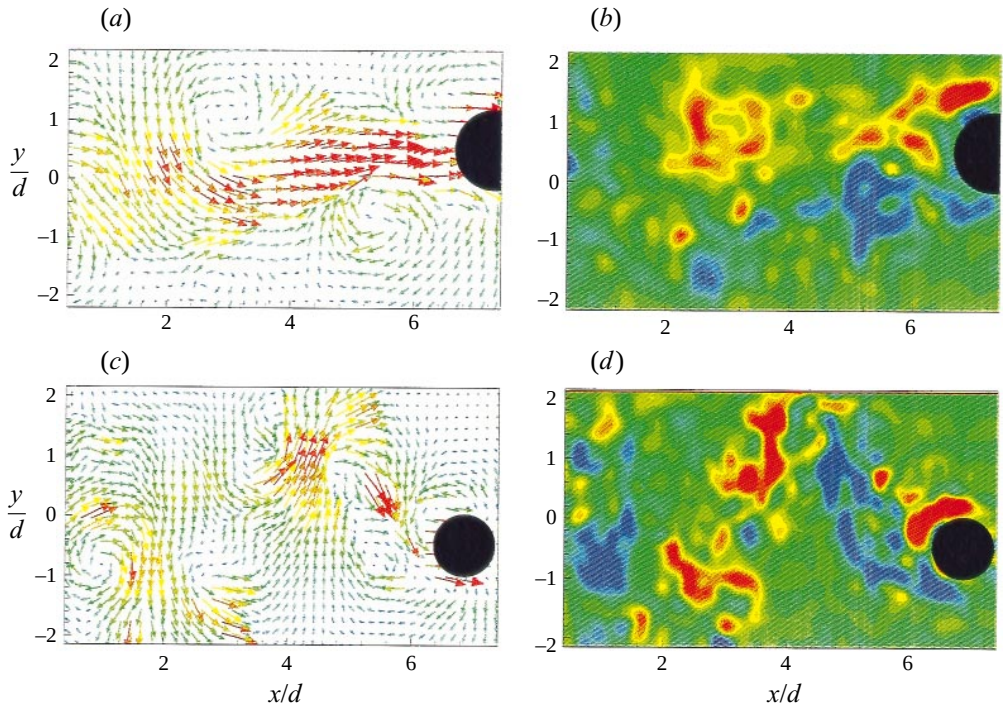

FIGURE 13. Velocity and vorticity plots: (*a*, *b*) $z/\overline{d} = 22.9$; and (*c*, *d*) $z/\overline{d} = 7.9$; for $R_{\overline{d}} = 1500$, $A/\overline{d} = 0.5$, and $f^* = 0.198$.

Figure 15 provides a sketch of the topology of primary vortex reconnection as it emerges from the lead precipitation results. The figure shows a snapshot in the hybrid mode formation; the details of the individual '2S' and '2P' pattern formation and evolution, at sections lying at least two diameters away from the vortex split location, resemble closely the corresponding patterns shown by Williamson & Roshko for uniform cylinders.

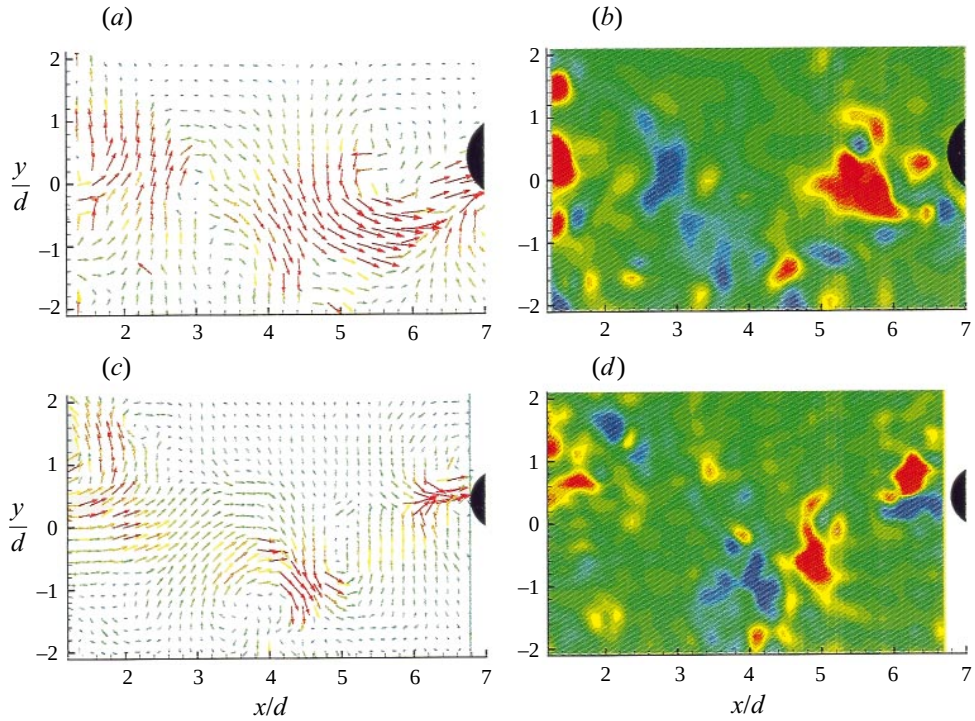

FIGURE 14. Velocity and vorticity plots: (a, b) $z/\overline{d} = 18.7$; and (c, d) $z/\overline{d} = 6.7$; for $R_{\overline{d}} = 1500$, $A/\overline{d} = 0.5$, and $f^* = 0.18$.

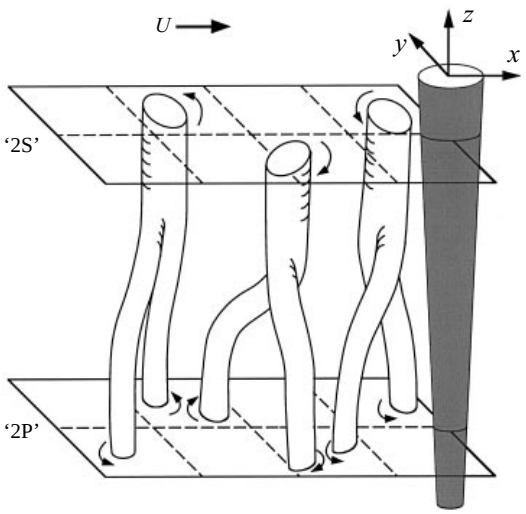

FIGURE 15. A sketch of the proposed 'hybrid' shedding mode suggests the topology of the vortex reconnection between the '2S' mode at the larger diameter end and the '2P' mode at the smaller diameter end.

4. Conclusions

Flow visualization behind a linearly tapered, oscillating cylinder, with average diameter $\overline{d}$ and taper ratio 4:1, was conducted at Reynolds numbers in the range 400–1500. The results reveal that within a certain parametric range a *hybrid mode* forms, consisting of the simultaneous formation of two different primary vortical patterns along the span of the cylinder: (*a*) two vortices per cycle ('2S' pattern) along the part with the larger diameter; and (*b*) four vortices per cycle ('2P' pattern) along the part with the smaller diameter. The transition between the two patterns occurs at a specific spanwise location, whose position depends on the amplitude to diameter ratio $A/\overline{d}$, the reduced frequency $f^* = f\overline{d}/U$, and the Reynolds number $Re_{\overline{d}} = U\overline{d}/\nu$. The two patterns of the mode are phase-locked, and the mode is periodic and persistent, hence there is no low-frequency forcing; in this sense it is different than the vortex dislocation observed behind non-uniform cylinders, such as reviewed in Williamson (1996*b*). A vortex connection topology is suggested on the basis of lead precipitation and DPIV data.

Outside the range of hybrid mode formation clean '2S' or '2P' modes are observed. Streamwise vortices are ubiquitous for all Reynolds numbers considered, irrespective of amplitude and frequency of oscillation, or the specific mode of vortex shedding.

Financial support has been provided by the Office of Naval Research (Ocean Engineering Division), under contract N00014-95-1-0106, monitored by Dr T. F. Swean, Jr.

REFERENCES

Adrian, R. J. 1991 Particle imaging techniques for experimental fluid mechanics. *Ann. Rev. Fluid Mech.* **23**, 261–304.

Anderson, E. A. & Szewczyk, A. A. 1995 Vortex shedding from a straight and tapered circular cylinder in uniform and shear flow. *Proc. Sixth Intl Conf. on Flow Induced Vibration*, pp. 61–71.

Bays-Muchmore, B. & Ahmed, A. 1993 On streamwise vortices in turbulent wakes of cylinders. *Phys. Fluids* A **5**, 387–392.

Bishop, R. E. D. & Hassan, A. Y. 1964 The lift and drag forces on a circular cylinder oscillating in a flowing fluid. *Proc. R. Soc. Lond.* A **277**, 51–75.

Bloor, M. S. 1964 The transition to turbulence in the wake of a circular cylinder. *J. Fluid Mech.* **19**, 290–304.

Brika, D. & Laneville, A. 1993 Vortex–induced vibrations of a long flexible circular cylinder. *J. Fluid Mech.* **250**, 481–508.

Chyu, C. & Rockwell, D. 1996 Evolution of patterns of streamwise vorticity in the turbulent wake of a circular cylinder *J. Fluid Mech.* **320**, 117–137.

Coutanceau, M. & Defaye, J. R. 1991 Circular cylinder wake configurations: A flow visualization survey. *Appl. Mech. Rev.* **44**, 255–305.

Eisenlohr, H. & Eckelmann, H. 1989 Vortex splitting and it consequences in the vortex street wake of cylinders at low Reynolds numbers. *Phys. Fluids* A **1**, 189–192.

Feng, C. C. 1968 The measurement of vortex–induced effects in flow past stationary and oscillating circular and D–section cylinders. M.A.Sc. Thesis, University of British Columbia.

Gaster, M. 1969 Vortex shedding from slender cones at low Reynolds numbers. *J. Fluid Mech.* **38**, 565–576.

Gaster, M. 1971 Vortex shedding from circular cylinders at low Reynolds numbers. *J. Fluid Mech.* **46**, 746–756.

Gerrard, J. H. 1978 The wakes of cylindrical bluff bodies at low Reynolds number. *Phil. Trans. R. Soc. Lond.* **288**, 351–378.

Gopalkrishnan, R., Triantafyllou, M. S., Triantafyllou, G. S. & Barrett, D. 1994 Active vorticity control in a shear flow using a flapping foil. *J. Fluid Mech.* **274**, 1–21.

Honji, H., Taneda, S. & Tatsuno, M. 1980 Some practical details of the electrolytic precipitation method of flow visualization. *Rep. Res. Inst. Appl. Math* **28**, 83–89.

Karniadakis, G. E. & Triantafyllou, G. S. 1992 Three-dimensional dynamics and transition to turbulence in the wake of bluff objects. *J. Fluid Mech.* **238**, 1–30.

Lin, J. C., Vorobieff, P. & Rockwell, D. 1996 Space–time imaging of a turbulent near–wake by high–image–density particle image cinematography. *Phys. Fluids* **8**, 555–564.

Nakano, M. & Rockwell, D. 1994 Flow structure in the frequency–modulated wake of a cylinder. *J. Fluid Mech.* **266**, 93–19.

Noack, B. N., Ohle, F. & Eckelmann, H. 1991 On cell formation in vortex streets. *J. Fluid Mech.* **227**, 293–308.

Ongoren, A. & Rockwell, D. 1988 *a* Flow structure from an oscillating cylinder. Part 1. Mechanics of phase shift and recovery in the near wake. *J. Fluid Mech.* **191**, 197–223.

Ongoren, A. & Rockwell, D. 1988 *b* Flow structure from an oscillating cylinder. Part 2. Mode competition in the near wake. *J. Fluid Mech.* **191**, 225–245.

Papangelou, A. 1992 Vortex shedding from slender cones at low Reynolds numbers. *J. Fluid Mech.* **242**, 299–321.

Piccirillo, P. S. & Van Atta, C. W. 1993 An experimental study of vortex shedding behind linearly tapered cylinders at low Reynolds number. *J. Fluid Mech.* **246**, 163–195.

Prasad, A. & Williamson, C. H. K. 1997 The instability of a shear layer separating from a bluff body. *J. Fluid Mech.* **333**, 375–402.

Roshko, A. 1954 On the development of turbulent wakes from vortex streets. *NACA Rep.* **1191**, 1–23.

Slaouti, A. & Gerrard, J. H. 1981 An experimental investigation of the end effects on the wake of a circular cylinder towed through water at low Reynolds numbers. *J. Fluid Mech.* **112**, 297–314.

Stansby, P. K. 1976 The locking-on of vortex shedding due to the cross-stream vibration of circular cylinders in uniform and shear flows. *J. Fluid Mech.* **74**, 641–655.

Szepessy, S. 1994 On the spanwise correlation of vortex shedding from a circular cylinder at high subcritical Reynolds number. *Phys. Fluids* **6**, 2406–2416.

Towfighi, J. & Rockwell, D. 1994 Flow structure from an oscillating nonuniform cylinder: Generation of patterned vorticity concentrations. *Phys. Fluids* **6**, 531–536.

Triantafyllou, G. S. 1992 Three–dimensional flow patterns in two dimensional wakes. *Trans. ASME: J. Fluids Engng* **114**, 356–361.

Wei, T. & Smith, C. R. 1986 Secondary vortices in the wake of circular cylinders. *J. Fluid Mech.* **169**, 513–533.

Willert, C. E. & Gharib, M. 1991 Digital particle image velocimetry. *Exps. Fluids* **10**, 181–193.

Williamson, C. H. K. 1992 The natural and forced formation of spot-like 'vortex dislocations' in the transition of a wake. *J. Fluid Mech.* **243**, 393–441.

Williamson, C. H. K. 1996 *a*, Three-dimensional wake transition *J. Fluid Mech.* **328**, 345–407.

Williamson, C. H. K. 1996 *b*, Vortex dynamics in the wake. *Ann. Rev. Fluid Mech.* **28**, 477–539.

Williamson, C. H. K. & Roshko, A. 1988 Vortex formation in the wake of an oscillating cylinder. *J. Fluids Struct.* **2**, 355–381.

Wu, J., Sheridan, J., Welsh, M. C. & Houridan, K. 1996 Three-dimensional vortex structures in a cylinder wake. *J. Fluid Mech.* **312**, 201–222.

Wu, J., Sheridan, J., Welsh, M. C., Houridan, K. & Thompson, M. 1994 Longitudinal vortex structures in a cylinder wake. *Phys. Fluids* **6**, 2883-2885.

Zhang, H. Q., Fey, U., Noack, B. R., Konig, M. & Eckelmann, H. 1995 On the transition of the cylinder wake. *Phys. Fluids* **7**, 779–794.

Zhou, Y. & Antonia, A. 1994 Critical points in a turbulent near wake. *J. Fluid Mech.* **275**, 59–81.